

TwistNet-2D: Learning Second-Order Channel Interactions via Spiral Twisting for Texture Recognition

Junbo Jacob Lian¹, Feng Xiong¹, Yujun Sun¹, Kaichen Ouyang², Zong Ke³, Mingyang Yu⁴, Shengwei Fu⁵, Rui Zhong⁶, Yujun Zhang⁷, and Huiling Chen⁸

¹Northwestern University ²Johns Hopkins University ³National University of Singapore ⁴Nankai University ⁵Guizhou University ⁶Hokkaido University
⁷Jingchu University of Technology ⁸Wenzhou University

Abstract. Second-order feature statistics are central to texture recognition, yet current methods face a fundamental tension: bilinear pooling and Gram matrices capture global channel correlations but collapse spatial structure, while self-attention models spatial context through weighted aggregation rather than explicit pairwise feature interactions. We introduce TwistNet-2D, a lightweight module that computes *local* pairwise channel products under *directional spatial displacement*, jointly encoding where features co-occur and how they interact. The core component, Spiral-Twisted Channel Interaction (STCI), shifts one feature map along a prescribed direction before element-wise channel multiplication, thereby capturing the cross-position co-occurrence patterns characteristic of structured and periodic textures. Aggregating four directional heads with learned channel reweighting and injecting the result through a sigmoid-gated residual path, TwistNet-2D incurs only $\sim 3.5\%$ additional parameters and $\sim 2\%$ additional FLOPs over ResNet-18, yet consistently surpasses both parameter-matched and substantially larger baselines—including ConvNeXt, Swin Transformer, and hybrid CNN–Transformer architectures—across four texture and fine-grained recognition benchmarks. Code is available at <https://github.com/junbolian/TwistNet-2D>.

Keywords: Texture recognition · Second-order features · Channel interaction · Classification · Lightweight networks

1 Introduction

Texture recognition demands understanding *how* visual features relate, not merely *what* features are present. Consider wood grain: its identity emerges from the alternation of dark stripes and light bands at regular intervals—a pattern defined by the *co-occurrence* of features at specific *spatial offsets*. This insight is classical: Haralick’s gray-level co-occurrence matrices [1] explicitly count feature pairs at spatial displacements, capturing the periodic structure that distinguishes one

texture from another. The challenge for modern deep networks is incorporating this principle—explicit, spatially-aware co-occurrence modeling—without sacrificing the flexibility of learned representations.

Existing approaches to second-order feature modeling face a fundamental tension between *what* they capture and *what* they discard:

- **Bilinear pooling** [2,3] and **Gram matrices** [4] compute products $\sum_{x,y} z_i(x,y) \cdot z_j(x,y)$, summing over all positions. This captures *that* features co-occur, but not *where*—yet for textures like stripes or grids, spatial arrangement is precisely what matters.
- **Self-attention** [5] models cross-position relationships, but through weighted sums $\sum_j \alpha_{ij} v_j$, not products. Weighted sums re-combine existing features; products create *new* second-order features that explicitly represent co-occurrence. These are fundamentally different operations with different representational power.
- **Same-position products** (local bilinear) compute $z_i(x,y) \cdot z_j(x,y)$ at each location, preserving spatial structure. But for periodic textures, correlated features often appear at *neighboring* positions—stripes and gaps alternate spatially. Same-position products miss this cross-position correlation entirely.

The gap is now precise: we need second-order features that are (1) computed *locally* to preserve spatial structure, and (2) capture *cross-position* correlations to model periodic patterns. No existing method provides both.

Our insight. The solution is to compute products between a feature at position (x,y) and a *directionally-displaced* feature at $(x+\delta, y+\delta)$:

$$\phi_{ij}(x,y) = \bar{z}_i(x,y) \cdot \bar{z}_j(x+\delta, y+\delta), \quad (1)$$

where \bar{z} denotes ℓ_2 -normalized features. This single operation achieves both goals: the product is computed per-position (preserving locality), while the displacement captures cross-position correlation (modeling periodicity). Unlike global pooling, we retain *where* co-occurrences happen; unlike same-position products, we capture *how* features relate across space.

We instantiate this insight as **Spiral-Twisted Channel Interaction (STCI)**. The “twist” refers to the directional displacement: we shift one operand via a learnable 3×3 depthwise convolution initialized to sample from a specific direction. By aggregating four directions ($0^\circ, 45^\circ, 90^\circ, 135^\circ$), we capture periodic structures at any orientation. Channel reduction ($C \rightarrow 8$) before products keeps computation tractable; Adaptive Interaction Selection (AIS) applies SE-style attention [6] to the resulting interaction channels, selecting which co-occurrence patterns matter for each image. A sigmoid-gated residual connection, initialized near zero, enables stable integration into pretrained networks.

Why this works. The design connects to information theory: for Gaussian features, mutual information $I(Z_i; Z_j) \propto -\log(1 - \rho_{ij}^2)$ depends on correlation ρ_{ij} .

Our normalized products estimate this correlation directly. The directional displacement extends this to *cross-position* mutual information, quantifying how much knowing $z_i(x, y)$ tells us about $z_j(x+\delta, y+\delta)$ —exactly the statistical structure that defines periodic textures. This theoretical grounding explains why explicit second-order products outperform implicit learning: they directly compute the statistics that matter, rather than hoping the network discovers them through gradient descent.

Contributions.

- We identify a specific gap in texture representation: existing methods either discard spatial structure (global pooling) or miss cross-position correlations (same-position products). We propose **STCI**, which addresses both through directionally-displaced pairwise products (§3.2).
- We introduce **Adaptive Interaction Selection**, applying channel attention to second-order features rather than raw features. This enables content-dependent weighting of co-occurrence patterns—emphasizing stripe correlations for wood, grid correlations for fabric (§3.3).
- We design a **gated integration** scheme with near-zero initialization, enabling stable insertion of second-order branches into pretrained CNNs without disrupting learned representations (§3.4).
- We conduct **comprehensive experiments** on four benchmarks spanning texture and fine-grained recognition. TwistNet-18 consistently outperforms parameter-matched baselines and remains competitive with or surpasses models $2.4\times$ its size, with only $\sim 3.5\%$ parameter overhead over ResNet-18—demonstrating that explicit co-occurrence modeling is particularly effective in data-limited, train-from-scratch settings where larger architectures fail to generalize (§4).

2 Related Work

Second-order representations. The importance of second-order statistics for texture is established theoretically [7, 8] and practically [1]. Gram matrices enable neural style transfer by matching texture statistics [4, 9, 10]. Bilinear pooling [2] computes outer products for fine-grained recognition, with efficient variants via compact projections [3], low-rank factorization [11], or covariance normalization [12]. Sikdar *et al.* [13] recently explored high-order interactions. All these methods pool spatially before computing statistics, losing the spatial structure we preserve. Our local, cross-position products provide complementary information: not just *that* features co-occur, but *where* and *at what offset*.

Texture recognition. Deep texture recognition evolved from CNN features with orderless pooling [14, 15] to specialized architectures. Zhai *et al.* [16] proposed multi-scale structural aggregation; their follow-up [17] explored primitive multiplicity for wild textures. Evani *et al.* [18] introduced spectral attention mechanisms. These methods improve feature extraction or attention design; we take a

different approach by explicitly modeling the co-occurrence statistics that define texture, connecting modern deep learning to classical texture analysis principles.

Attention mechanisms. Self-attention [5] was adapted to vision [19] with efficient variants using local windows [20], linear approximations [21], or hybrid designs [22,23]. Channel attention [6,24–26] reweights features via global statistics. The key distinction: attention computes weighted sums over existing features, while we compute products that create new interaction features. Our AIS applies attention to these interaction channels, selecting which co-occurrence patterns to emphasize—complementary to standard attention.

Backbones and polynomial networks. Modern CNNs [27–30] provide strong baselines. TwistNet-2D is designed as a complementary module, insertable with minimal modification. Polynomial networks [31] motivate explicit higher-order expansions; STCI can be viewed as a spatially-aware quadratic expansion with aggressive bottlenecking. Our prior work [32] introduced twisted interactions for tabular data; TwistNet-2D extends this to images, where the “twist” becomes directional spatial displacement—capturing the cross-position structure unique to visual textures.

3 Method

Figure 1 provides an overview of TwistNet-2D. We begin with theoretical motivation (§3.1), then describe the Spiral-Twisted Channel Interaction module (§3.2), multi-head aggregation with adaptive selection (§3.3), residual integration (§3.4), and the full architecture (§3.5).

3.1 Motivation: Why Explicit Second-Order Interactions?

Information-theoretic perspective. For jointly Gaussian random variables, mutual information is determined by correlation:

$$I(Z_i; Z_j) = -\frac{1}{2} \log(1 - \rho_{ij}^2), \quad (2)$$

where $\rho_{ij} = \mathbb{E}[\bar{z}_i \cdot \bar{z}_j]$ is the correlation coefficient between ℓ_2 -normalized features. When features deviate from Gaussianity, (2) provides a lower bound on mutual information. Our normalized pairwise products $\bar{z}_i \cdot \bar{z}_j$ directly estimate this correlation, providing an efficient proxy for the statistical dependence between channels.

From global to local Gram matrices. Neural style transfer [4] captures texture via the global Gram matrix $G_{ij} = \sum_{hw} F_{ihw} F_{jhw}$, which aggregates co-occurrence statistics across all spatial positions. While effective for style matching, this global pooling discards *where* features co-occur—information that can be discriminative for recognition. Our approach computes *local* Gram-like products $z_i(x, y) \cdot z_j(x, y)$ at each position, preserving spatial structure.

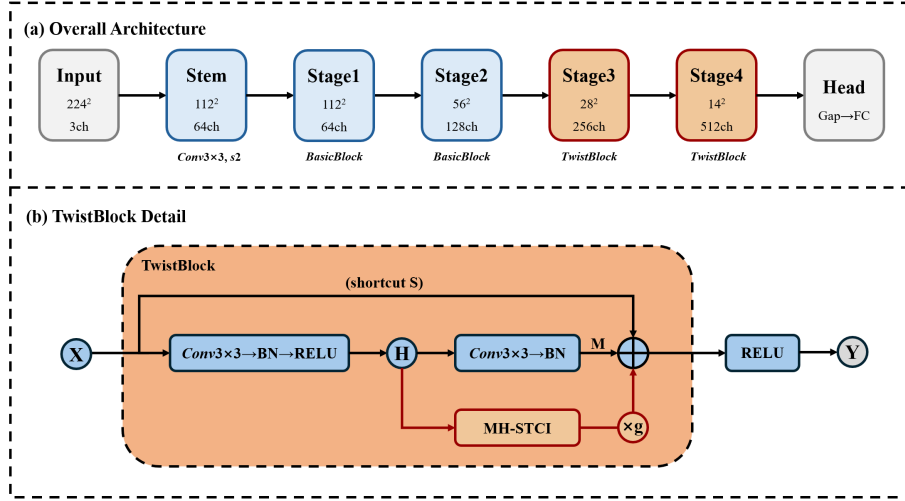


Fig. 1: TwistNet-2D architecture. (Top) TwistNet-2D-18 follows a ResNet-like structure with four stages; Stages 3–4 use TwistBlocks that inject second-order channel interactions. (Bottom) TwistBlock augments the standard residual block with a gated MH-STCI branch.

Cross-position correlations. Texture patterns often exhibit spatial periodicity: correlated features appear at neighboring rather than identical positions. Consider wood grain, where stripe patterns alternate with brown regions at regular intervals. Same-position products $z_i(x, y) \cdot z_j(x, y)$ miss this periodic structure because stripe and brown detectors peak at different locations. Our *spiral twist* addresses this by computing cross-position products $z_i(x, y) \cdot \tilde{z}_j(x+\delta, y+\delta)$, where \tilde{z} is spatially displaced. This design parallels Haralick’s gray-level co-occurrence matrices [1], which count feature pairs at specified spatial offsets—but implemented as a learnable, end-to-end differentiable module.

3.2 Spiral-Twisted Channel Interaction (STCI)

Given an intermediate feature map $X \in \mathbb{R}^{C \times H \times W}$, STCI computes local second-order interactions with directional displacement. Figure 3 illustrates the module; Figure 2 visualizes why cross-position products capture texture periodicity.

Step 1: Channel reduction. To limit computational cost, we first compress channels via a 1×1 convolution:

$$Z = \text{ReLU}(\text{BN}(W_{\text{red}} * X)), \quad W_{\text{red}} \in \mathbb{R}^{C_r \times C \times 1 \times 1}, \quad (3)$$

where $C_r \ll C$ (we use $C_r = 8$). This reduces the number of pairwise products from $O(C^2)$ to $O(C_r^2)$.

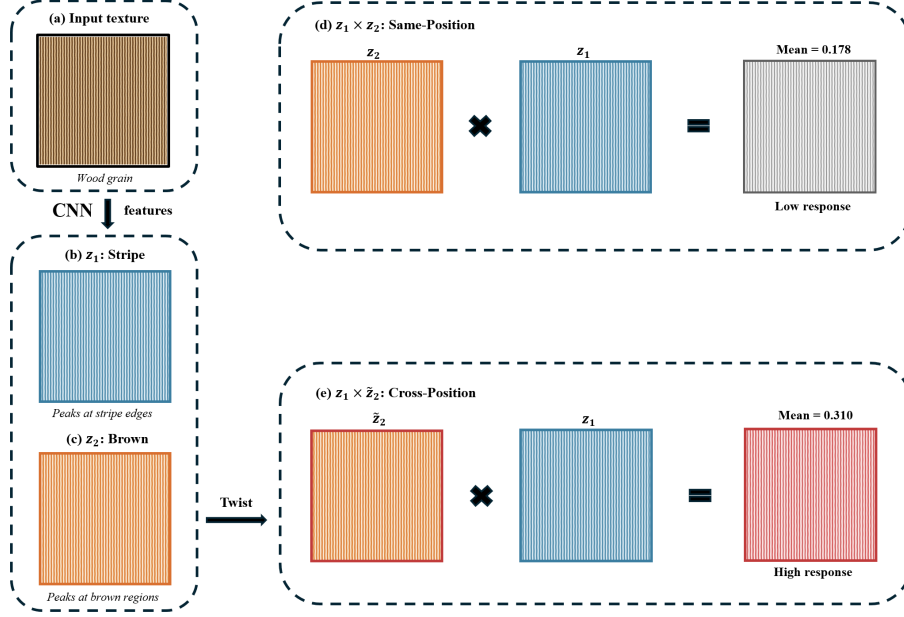


Fig. 2: Why cross-position correlation? (a) Wood grain exhibits periodic stripe-brown alternation. (b)–(c) CNN extracts stripe detector z_1 and brown detector z_2 . (d) Same-position product $z_1 \times z_2$ yields low response due to misaligned peaks. (e) Spiral Twist shifts z_2 by δ ; the cross-position product $z_1 \times \tilde{z}_2$ aligns peaks, capturing periodicity.

Step 2: Directional spiral twist. We apply a directional spatial displacement via depthwise convolution:

$$\tilde{Z} = \text{DWConv}_\theta(Z) \odot s, \quad (4)$$

where θ indexes one of four directions, $s \in \mathbb{R}^{C_r}$ is a learnable per-channel scale (initialized to ones), and DWConv_θ is a 3×3 depthwise convolution with direction-specific initialization.

Each kernel $\mathbf{K}^\theta \in \mathbb{R}^{3 \times 3}$ is initialized to sample from the center and one directionally-offset neighbor:

$$\mathbf{K}^\theta[1, 1] = 0.5, \quad \mathbf{K}^\theta[1 + \delta_y, 1 + \delta_x] = 0.5, \quad (5)$$

with all other entries zero. The offsets are $(\delta_x, \delta_y) = (\text{round}(\cos \theta), \text{round}(\sin \theta))$ for $\theta \in \{0, \frac{\pi}{4}, \frac{\pi}{2}, \frac{3\pi}{4}\}$. Table 1 shows the resulting kernels.

Why four directions? We use four directions spanning $[0, \pi]$ rather than all eight compass directions. After ℓ_2 normalization, $\tilde{z}_i \cdot \tilde{z}_j$ measures correlation, which is approximately symmetric for texture patterns: sampling from A toward B captures similar statistics as sampling from B toward A . Thus, opposite directions

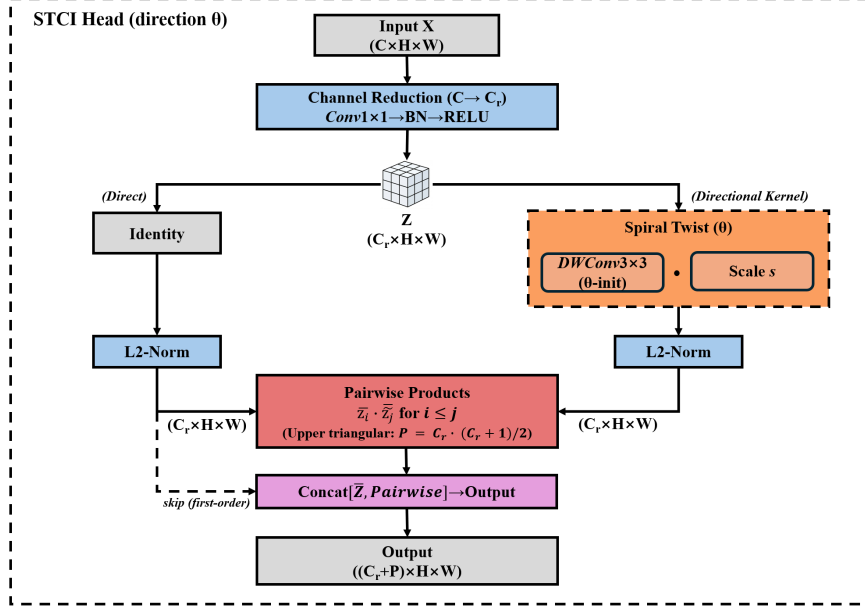


Fig. 3: Single STCI head. Channel reduction, directional spiral twist, ℓ_2 normalization, pairwise products, and output concatenation.

(0 vs. π , $\frac{\pi}{4}$ vs. $\frac{5\pi}{4}$, etc.) are redundant. Four directions cover horizontal, vertical, and both diagonal axes while halving computational cost. We verify this choice in §4.3.

Step 3: ℓ_2 normalization. We normalize features channel-wise to stabilize magnitudes and ensure products estimate correlations:

$$\bar{Z} = \frac{Z}{\|Z\|_2 + \epsilon}, \quad \tilde{Z} = \frac{\tilde{Z}}{\|\tilde{Z}\|_2 + \epsilon}, \quad (6)$$

where the norm is computed along the channel dimension at each spatial location ($\epsilon = 10^{-6}$).

Step 4: Pairwise products. We compute the upper-triangular set of pairwise products:

$$\phi(\bar{Z}, \tilde{Z}) = [\bar{z}_i \cdot \tilde{z}_j]_{1 \leq i \leq j \leq C_r} \in \mathbb{R}^{P \times H \times W}, \quad (7)$$

where $P = C_r(C_r+1)/2 = 36$ for $C_r = 8$. The upper-triangular constraint avoids redundant symmetric pairs while retaining diagonal terms ($\bar{z}_i \cdot \tilde{z}_i$).

Table 1: Directional kernel initialization. Each 3×3 kernel samples from center and one neighbor.

$\theta = 0$	$\theta = \frac{\pi}{4}$	$\theta = \frac{\pi}{2}$	$\theta = \frac{3\pi}{4}$
$\begin{bmatrix} 0 & 0 & 0 \\ 0.5 & 0.5 & 0 \\ 0 & 0 & 0 \end{bmatrix}$	$\begin{bmatrix} 0 & 0 & 0 \\ 0.5 & 0 & 0 \\ 0 & 0.5 & 0 \end{bmatrix}$	$\begin{bmatrix} 0 & 0 & 0 \\ 0.5 & 0 & 0 \\ 0 & 0.5 & 0 \end{bmatrix}$	$\begin{bmatrix} 0 & 0 & 0 \\ 0 & 0.5 & 0 \\ 0.5 & 0 & 0 \end{bmatrix}$
(\rightarrow)	(\nwarrow)	(\downarrow)	(\swarrow)

Output. A single STCI head outputs the concatenation of first-order and second-order features:

$$\text{STCI}_\theta(X) = [\bar{Z}; \phi(\bar{Z}, \tilde{Z})] \in \mathbb{R}^{(C_r+P) \times H \times W}. \quad (8)$$

Including \tilde{Z} enables the module to fall back to linear behavior when interactions are not beneficial.

Implementation. We implement pairwise products using precomputed index tensors. Let $\text{idx_i}, \text{idx_j} \in \{1, \dots, C_r\}^P$ store upper-triangular index pairs. The products are computed as $\phi = \bar{Z}[\text{idx_i}] \odot \tilde{Z}[\text{idx_j}]$, avoiding explicit loops.

3.3 Multi-Head Aggregation with Adaptive Selection

To achieve robustness to texture orientation, we aggregate STCI outputs from multiple directions (Figure 4).

Multi-head aggregation. We instantiate $K = 4$ STCI heads with directions $\theta_k \in \{0, \frac{\pi}{4}, \frac{\pi}{2}, \frac{3\pi}{4}\}$ and concatenate:

$$F = \bigoplus_{k=1}^K \text{STCI}_{\theta_k}(X) \in \mathbb{R}^{D \times H \times W}, \quad (9)$$

where $D = K(C_r + P) = 4 \times 44 = 176$ channels.

Adaptive Interaction Selection (AIS). Different images benefit from different interaction patterns. We apply SE-style attention [6] to dynamically weight interaction channels:

$$\text{AIS}(F) = F \odot \sigma(W_2 \cdot \text{ReLU}(W_1 \cdot \text{GAP}(F))), \quad (10)$$

where $\text{GAP}(\cdot)$ is global average pooling, $W_1 \in \mathbb{R}^{D_{\text{mid}} \times D}$, $W_2 \in \mathbb{R}^{D \times D_{\text{mid}}}$, and $D_{\text{mid}} = \max(D/4, 16)$. Unlike standard channel attention on raw features, AIS operates on *interaction channels*, selecting which co-occurrence patterns to emphasize.

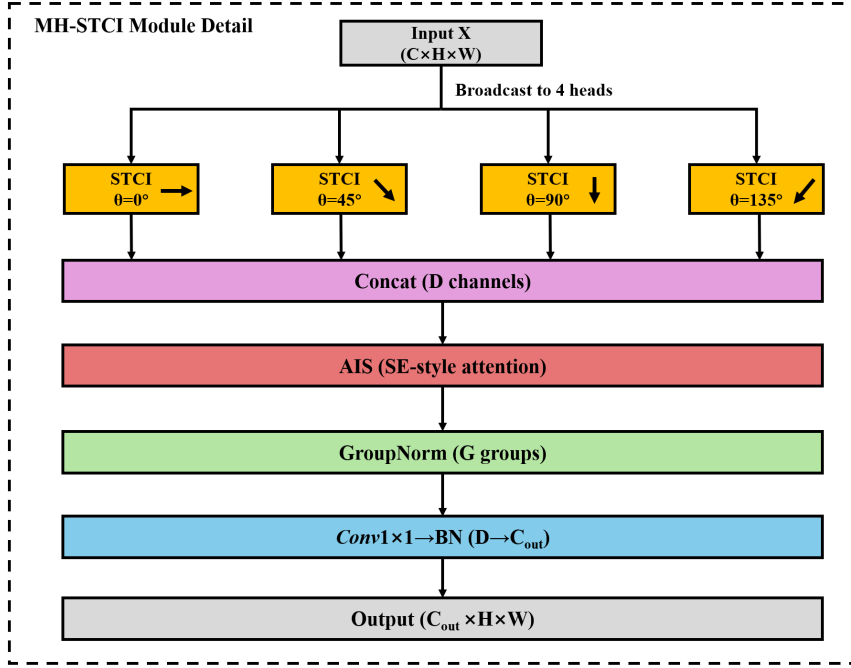


Fig. 4: Multi-Head STCI (MH-STCI). Four directional heads are concatenated, reweighted by AIS, normalized, and projected to output channels.

Normalization and projection. We apply GroupNorm [33] for stability across batch sizes, then project to output channels:

$$MH-STCI(X) = BN(W_{proj} * GN(AIS(F))), \quad (11)$$

where $W_{proj} \in \mathbb{R}^{C_{out} \times D \times 1 \times 1}$ is initialized with small random values ($std = 0.01$) to ensure near-zero output at initialization.

3.4 TwistBlock: Residual Integration

We integrate MH-STCI into ResNet BasicBlocks [27] via gated injection (Figure 1, bottom).

Backbone block. The standard BasicBlock computes:

$$H = \text{ReLU}(BN(W_1 * X)), \quad (12)$$

$$M = BN(W_2 * H), \quad (13)$$

where X is the input, H is the intermediate activation, and M is the main-path output.

Gated injection. We compute interactions from the intermediate representation H and inject via a learnable gate:

$$Y = \text{ReLU}(M + g \cdot \text{MH-STCI}(H) + S(X)), \quad (14)$$

where $S(\cdot)$ is identity or a 1×1 strided convolution (for resolution/channel changes), and $g = \sigma(\gamma)$ is a sigmoid-gated scalar.

Gate initialization. We initialize $\gamma = -2.0$, yielding $g \approx 0.12$. This “soft start” ensures the block initially behaves like a standard ResNet block, preserving stable gradient flow. During training, g can increase to exploit interactions when beneficial, or remain small if interactions are unhelpful.

3.5 Architecture and Complexity

TwistNet-2D-18. We adopt a ResNet-18-like structure with the standard ResNet stem (7×7 conv followed by 3×3 max pooling) and four stages with channel widths (64, 128, 256, 512) and two blocks per stage. Stages 1–2 use standard BasicBlocks; Stages 3–4 use TwistBlocks. This placement reflects that co-occurrence patterns are most discriminative at higher semantic levels, where features encode object parts rather than low-level edges. Global average pooling and a linear classifier follow the final stage.

Parameter overhead. Each TwistBlock adds $\sim 70K$ parameters for MH-STCI (reduction, twist, AIS, projection). With four TwistBlocks in Stages 3–4, total overhead is $\sim 0.4M$ parameters. TwistNet-2D-18 totals 11.59M parameters, approximately 3.5% more than ResNet-18 (11.20M).

Computational cost. Pairwise products add $O(P \cdot H \cdot W)$ multiplications per head. At Stage 3–4 resolutions (28×28 and 14×14), this is negligible compared to 3×3 convolutions. Overall FLOPs increase by $\sim 2\%$, from 1.82G (ResNet-18) to 1.85G (TwistNet-2D-18).

4 Experiments

We evaluate TwistNet-2D on four benchmarks to answer three questions: (1) Does explicit second-order modeling improve over first-order baselines? (2) How does TwistNet-2D compare to recent efficient architectures? (3) Which components contribute most to performance?

4.1 Experimental Setup

Datasets. We use four benchmarks: **DTD** [14] (5,640 images, 47 texture classes, 10-fold CV); **FMD** [34] (1,000 images, 10 materials, 5-fold CV); **CUB-200** [35] (11,788 images, 200 bird species, 5-fold CV); and **Flowers-102** [36] (8,189 images, 102 categories, 5-fold CV).

Table 2: Main results. All models trained from scratch without ImageNet pre-training. Mean accuracy (%) \pm std over folds and seeds. Best in **bold**, second-best underlined. † 28M params (2.4 \times larger); these overparameterized models suffer from severe overfitting on small-scale datasets without pretraining (see §4.2).

Model	Params	FLOPs	DTD	FMD	CUB-200	Flowers-102
<i>Group 1: Parameter-matched (10–16M)</i>						
ResNet-18	11.20M	1.82G	39.4 \pm 1.2	42.6 \pm 3.1	54.6 \pm 0.5	43.6 \pm 0.5
SE-ResNet-18	11.29M	1.82G	36.7 \pm 1.2	40.8 \pm 2.8	52.0 \pm 0.8	40.5 \pm 0.7
ConvNeXtV2-Nano	15.01M	2.45G	29.1 \pm 1.3	29.7 \pm 2.5	31.7 \pm 4.0	46.1 \pm 0.6
FastViT-SA12	10.60M	1.50G	<u>42.7\pm1.4</u>	45.0\pm3.6	49.9 \pm 0.6	59.9\pm0.6
RepViT-M1.5	13.67M	2.31G	39.2 \pm 1.5	36.6 \pm 2.2	<u>59.7\pm0.6</u>	51.6 \pm 0.7
TwistNet-18	11.59M	1.85G	45.8\pm1.4	<u>43.5\pm3.8</u>	61.8\pm0.5	<u>58.5\pm0.7</u>
<i>Group 2: Larger baselines (~28M)</i>						
ConvNeXt-Tiny †	27.86M	4.47G	11.1 \pm 0.8	24.3 \pm 2.7	3.2 \pm 1.4	7.5 \pm 0.3
Swin-Tiny †	27.56M	4.51G	32.2 \pm 1.2	35.9 \pm 3.2	33.0 \pm 1.0	48.8 \pm 0.3

Baselines. We compare two groups: (1) *Parameter-matched* (10–16M): ResNet-18 [27], SE-ResNet-18 [6], ConvNeXtV2-Nano [37], FastViT-SA12 [22], and RepViT-M1.5 [30]; (2) *Larger models* (~28M): ConvNeXt-Tiny [28] and Swin-Tiny [20].

Training protocol. All models are trained *from scratch* without ImageNet pre-training to isolate architectural contributions from transfer learning. We use: 200 epochs, SGD with Nesterov momentum (0.9), weight decay 10^{-4} , cosine LR schedule (initial 0.05, 10-epoch warmup), batch size 64, input 224×224 . Augmentation includes RandAugment [38], Mixup ($\alpha=0.8$), CutMix ($\alpha=1.0$), and label smoothing ($\epsilon=0.1$). We report mean accuracy \pm std over all folds and 3 seeds.

4.2 Main Results

Table 2 and Figure 5 summarize results on all benchmarks.

Parameter-matched comparison. TwistNet-2D-18 achieves the highest accuracy across all four benchmarks among 10–16M models. On DTD, it outperforms ResNet-18 by 6.4% and SE-ResNet-18 by 9.1%, demonstrating that explicit second-order interactions capture texture patterns more effectively than channel attention alone. Notably, ConvNeXtV2-Nano (34% more parameters) significantly underperforms all other baselines when trained from scratch, suggesting its advantages stem primarily from ImageNet pretraining rather than architectural design for textures.

Comparison with FastViT-SA12. We analyze performance differences through the lens of what discriminative features each dataset emphasizes. TwistNet-2D achieves the largest gains on DTD (+3.1%) and CUB-200 (+11.9%), both datasets where *local periodic patterns*—textile weaves and feather barbs—serve

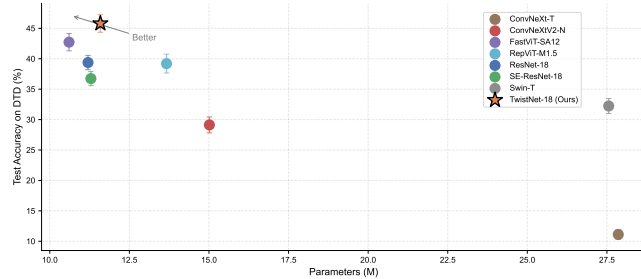


Fig. 5: Accuracy vs. parameters on DTD. TwistNet-18 achieves the highest accuracy among all models. Larger models (Group 2, ~ 28 M) suffer severe degradation without pretraining, underscoring the advantage of parameter-efficient designs in data-limited regimes.

as primary discriminative cues. In contrast, FastViT shows advantages on FMD (+1.5%) and Flowers-102 (+1.4%), where material reflectance and global color distributions play a more significant role than local co-occurrence statistics. This aligns with our design motivation: STCI explicitly computes pairwise correlations that capture periodic microstructures, whereas FastViT’s token mixing aggregates global context more effectively.

Effect of model scale without pretraining. Group 2 models (ConvNeXt-Tiny, Swin-Tiny) contain ~ 28 M parameters— $2.4\times$ more than Group 1—yet perform dramatically worse across all benchmarks. ConvNeXt-Tiny drops to 3.2% on CUB-200 and 11.1% on DTD, while Swin-Tiny reaches only 32.2% on DTD and 33.0% on CUB-200. This is consistent with well-documented observations that high-capacity architectures require large-scale pretraining to realize their potential [19, 28]: without ImageNet initialization, their excess capacity leads to severe overfitting on datasets with only a few thousand training images. The contrast is stark—TwistNet-2D-18 with 11.59M parameters outperforms ConvNeXt-Tiny (27.86M) by 34.7% on DTD and 58.6% on CUB-200—underscoring that architectural inductive bias, not raw model capacity, determines performance in data-limited regimes. This result highlights a practical advantage of lightweight, parameter-efficient designs: they generalize effectively without relying on large-scale pretraining.

Fine-grained recognition. On CUB-200, TwistNet-2D-18 (61.8%) outperforms all parameter-matched baselines by a substantial margin, exceeding FastViT-SA12 by 11.9% and RepViT-M1.5 by 2.1%. We attribute this to the nature of bird species discrimination: subtle differences in feather barb patterns and plumage striations are inherently *periodic microstructures* that STCI captures effectively. On Flowers-102, FastViT-SA12 (59.9%) marginally outperforms TwistNet-2D (58.5%) by 1.4%, as flower classification relies more on petal color gradients—features better characterized by global context aggregation. This dataset-dependent

Table 3: Ablation on DTD. Mean accuracy (%) \pm std over 10 folds \times 3 seeds.

Variant	Params	Acc.
TwistNet-18 (Full)	11.59M	45.8\pm1.4
w/o Spiral Twist	11.59M	45.6 \pm 1.5
w/o AIS	11.53M	44.1 \pm 1.8
First-order only	11.20M	39.4 \pm 1.2

behavior validates that TwistNet-2D provides targeted inductive bias for texture-discriminative tasks.

4.3 Ablation Study

Table 3 ablates key components on DTD.

Second-order interactions yield the largest gain. Removing all STCI modules (“First-order only”) reduces accuracy by 6.4%, confirming that explicit second-order features provide substantial benefits. This variant equals ResNet-18, demonstrating that the performance gap is entirely attributable to our proposed modules.

AIS contributes 1.7% accuracy. Adaptive Interaction Selection enables content-dependent weighting of co-occurrence patterns; without it, all directions contribute equally regardless of image content, reducing discriminability for textures with dominant orientations.

Spiral twist shows marginal improvement (0.2%) on DTD. This suggests that same-position channel interactions capture most discriminative information on DTD’s diverse categories.

4.4 Analysis

Learned interaction patterns. Figure 6 visualizes the channel interaction matrices from STCI on DTD samples with distinct orientation characteristics. For the vertical stripe texture (top row), the 0° direction head shows the strongest activation ($\mu=0.06$), capturing horizontal co-occurrence patterns perpendicular to the stripe orientation. The diagonal stripe texture (middle row) activates the 45° head most strongly ($\mu=0.06$), aligning with its dominant orientation. The scaly texture (bottom row) shows peak response at 135° ($\mu=0.04$), corresponding to the diagonal arrangement of scales. These results confirm that STCI automatically learns orientation-selective co-occurrence detectors without explicit supervision.

Computational overhead. STCI adds only 3.5% parameters and 1.6% FLOPs compared to the ResNet-18 backbone, while providing 6.4% accuracy improvement on DTD. This favorable trade-off makes TwistNet-2D practical for resource-constrained deployment.

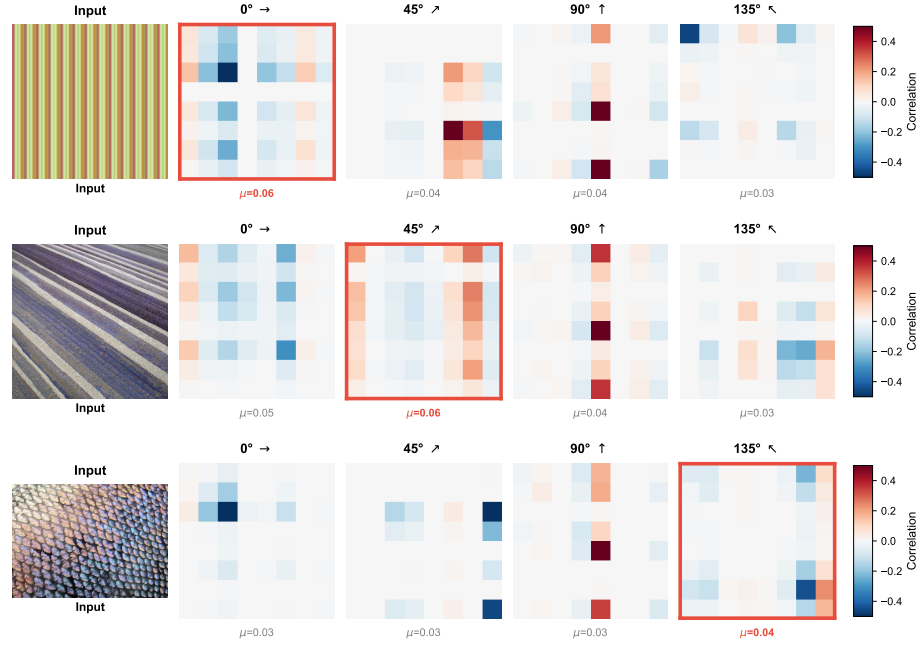


Fig. 6: Learned direction selectivity. Channel interaction matrices for three DTD textures. Each row shows one sample; columns display the four directional heads (0° , 45° , 90° , 135°). Red borders and bold μ values indicate the strongest responding direction. Textures with different dominant orientations activate corresponding directional heads.

Limitations. TwistNet-2D underperforms FastViT on FMD (43.5% vs. 45.0%) and Flowers-102 (58.5% vs. 59.9%), where global appearance statistics complement local co-occurrence. This suggests STCI’s fixed-direction, local-window design may miss information at larger spatial scales. Additionally, four canonical directions (0° , 45° , 90° , 135°) may suboptimally represent textures with arbitrary orientations. Learnable direction selection and multi-scale interactions are promising extensions. We also note that our train-from-scratch protocol, while isolating architectural contributions, precludes direct comparison with pre-trained models; evaluating TwistNet-2D with ImageNet initialization is an important direction for future work.

5 Conclusion

We presented TwistNet-2D, a lightweight architecture that incorporates explicit second-order channel interactions into CNNs via Spiral-Twisted Channel Interaction (STCI) modules. By computing pairwise feature correlations along multiple directions and adaptively weighting them through AIS, TwistNet-2D captures the co-occurrence statistics that characterize texture patterns. Experiments

on four benchmarks demonstrate that TwistNet-18 consistently outperforms parameter-matched baselines in the train-from-scratch setting, while overparameterized models ($2.4\times$ larger) suffer severe degradation without pretraining—underscoring the value of targeted inductive bias over raw model capacity in data-limited regimes. Visualization confirms that STCI learns interpretable, orientation-selective representations. Future work includes learnable direction selection, multi-scale interactions, and evaluation with pretrained initialization to assess complementarity with transfer learning.

References

1. Robert M. Haralick, K. Shanmugam, and Its’Hak Dinstein. Textural features for image classification. *IEEE Trans. Syst. Man Cybern.*, 12(6):610–621, 2007.
2. Tsung-Yu Lin, Aruni RoyChowdhury, and Subhransu Maji. Bilinear CNN models for fine-grained visual recognition. In *ICCV*, pages 1449–1457, 2015.
3. Yang Gao, Oscar Beijbom, Ning Zhang, and Trevor Darrell. Compact bilinear pooling. In *CVPR*, pages 317–326, 2016.
4. Leon A. Gatys, Alexander S. Ecker, and Matthias Bethge. Image style transfer using convolutional neural networks. In *CVPR*, pages 2414–2423, 2016.
5. Ashish Vaswani, Noam Shazeer, Niki Parmar, Jakob Uszkoreit, Llion Jones, Aidan N. Gomez, Łukasz Kaiser, and Illia Polosukhin. Attention is all you need. In *NeurIPS*, pages 5998–6008, 2017.
6. Jie Hu, Li Shen, and Gang Sun. Squeeze-and-excitation networks. In *CVPR*, pages 7132–7141, 2018.
7. Bela Julesz. Textons, the elements of texture perception, and their interactions. *Nature*, 290(5802):91–97, 1981.
8. Javier Portilla and Eero P. Simoncelli. A parametric texture model based on joint statistics of complex wavelet coefficients. *IJCV*, 40(1):49–70, 2000.
9. Justin Johnson, Alexandre Alahi, and Li Fei-Fei. Perceptual losses for real-time style transfer and super-resolution. In *ECCV*, pages 694–711, 2016.
10. Yanghao Li, Naiyan Wang, Jiaying Liu, and Xiaodi Hou. Demystifying neural style transfer. In *IJCAI*, pages 2230–2236, 2017.
11. Shu Kong and Charless Fowlkes. Low-rank bilinear pooling for fine-grained classification. In *CVPR*, pages 365–374, 2017.
12. Peihua Li, Jiangtao Xie, Qilong Wang, and Zilin Gao. Is second-order information helpful for large-scale visual recognition? In *ICCV*, pages 2070–2078, 2017.
13. Arindam Sikdar, Yonghuai Liu, Siddhardha Kedarisetty, Yitian Zhao, Amr Ahmed, and Ardhendu Behera. Interweaving insights: High-order feature interaction for fine-grained visual recognition. *IJCV*, 133(4):1755–1779, 2025.
14. Mircea Cimpoi, Subhransu Maji, Iasonas Kokkinos, Sammy Mohamed, and Andrea Vedaldi. Describing textures in the wild. In *CVPR*, pages 3606–3613, 2014.
15. Mircea Cimpoi, Subhransu Maji, and Andrea Vedaldi. Deep filter banks for texture recognition and segmentation. In *CVPR*, pages 3828–3836, 2015.
16. Wei Zhai, Yang Cao, Zheng-Jun Zha, HaiYong Xie, and Feng Wu. Deep structure-revealed network for texture recognition. In *CVPR*, pages 11010–11019, 2020.
17. Wei Zhai, Yang Cao, Jing Zhang, Haiyong Xie, Dacheng Tao, and Zheng-Jun Zha. On exploring multiplicity of primitives and attributes for texture recognition in the wild. *IEEE TPAMI*, 2023.

18. Ravishankar Evani, Deepu Rajan, and Shangbo Mao. Chebyshev attention depth permutation texture network with latent texture attribute loss. In *CVPR*, pages 23423–23432, 2025.
19. Alexey Dosovitskiy, Lucas Beyer, Alexander Kolesnikov, Dirk Weissenborn, Xiaohua Zhai, Thomas Unterthiner, Mostafa Dehghani, Matthias Minderer, Georg Heigold, Sylvain Gelly, Jakob Uszkoreit, and Neil Houlsby. An image is worth 16x16 words: Transformers for image recognition at scale. In *ICLR*, 2021.
20. Ze Liu, Yutong Lin, Yue Cao, Han Hu, Yixuan Wei, Zheng Zhang, Stephen Lin, and Baining Guo. Swin transformer: Hierarchical vision transformer using shifted windows. In *ICCV*, pages 10012–10022, 2021.
21. Angelos Katharopoulos, Apoorv Vyas, Nikolaos Pappas, and François Fleuret. Transformers are RNNs: Fast autoregressive transformers with linear attention. In *ICML*, pages 5156–5165, 2020.
22. Pavan Kumar Anasosalu Vasu, James Gabriel, Jeff Zhu, Oncel Tuzel, and Anurag Ranjan. Fastvit: A fast hybrid vision transformer using structural reparameterization. In *ICCV*, pages 5785–5795, 2023.
23. Zhengzhong Tu, Hossein Talebi, Han Zhang, Feng Yang, Peyman Milanfar, Alan Bovik, and Yinxiao Li. Maxvit: Multi-axis vision transformer. In *ECCV*, pages 459–479, 2022.
24. Sanghyun Woo, Jongchan Park, Joon-Young Lee, and In So Kweon. CBAM: Convolutional block attention module. In *ECCV*, pages 3–19, 2018.
25. Qilong Wang, Banggu Wu, Pengfei Zhu, Peihua Li, Wangmeng Zuo, and Qinghua Hu. ECA-Net: Efficient channel attention for deep convolutional neural networks. In *CVPR*, pages 11534–11542, 2020.
26. Qibin Hou, Daquan Zhou, and Jiashi Feng. Coordinate attention for efficient mobile network design. In *CVPR*, pages 13713–13722, 2021.
27. Kaiming He, Xiangyu Zhang, Shaoqing Ren, and Jian Sun. Deep residual learning for image recognition. In *CVPR*, pages 770–778, 2016.
28. Zhuang Liu, Hanzi Mao, Chao-Yuan Wu, Christoph Feichtenhofer, Trevor Darrell, and Saining Xie. A convnet for the 2020s. In *CVPR*, pages 11976–11986, 2022.
29. Mingxing Tan and Quoc V. Le. Efficientnet: Rethinking model scaling for convolutional neural networks. In *ICML*, pages 6105–6114, 2019.
30. Ao Wang, Hui Chen, Zijia Lin, Jungong Han, and Guiguang Ding. Repvit: Revisiting mobile cnn from vit perspective. In *CVPR*, pages 15909–15920, 2024.
31. Grigoris G. Chrysos, Stylianos Moschoglou, Giorgos Bouritsas, Yannis Panagakis, Jiankang Deng, and Stefanos Zafeiriou. Deep polynomial neural networks. *IEEE TPAMI*, 44(8):4021–4034, 2021.
32. Junbo Jacob Lian, Haoran Chen, Kaichen Ouyang, Yujun Zhang, Rui Zhong, and Huijing Chen. Twisted convolutional networks (TCNs): Enhancing feature interactions for non-spatial data classification. *Neural Networks*, 197:108451, May 2026.
33. Yuxin Wu and Kaiming He. Group normalization. In *ECCV*, pages 3–19, 2018.
34. Lavanya Sharan, Ruth Rosenholtz, and Edward H Adelson. Material perception: What can you see in a brief glance? *Journal of Vision*, 9(8):784–784, 2009.
35. Catherine Wah, Steve Branson, Peter Welinder, Pietro Perona, and Serge Belongie. The Caltech-UCSD birds-200-2011 dataset. Technical Report CNS-TR-2011-001, California Institute of Technology, 2011.
36. Maria-Elena Nilsback and Andrew Zisserman. Automated flower classification over a large number of classes. In *Indian Conference on Computer Vision, Graphics and Image Processing (ICVGIP)*, pages 722–729. IEEE, 2008.

37. Sanghyun Woo, Shoubhik Debnath, Ronghang Hu, Xinlei Chen, Zhuang Liu, In So Kweon, and Saining Xie. ConvNeXt V2: Co-designing and scaling ConvNets with masked autoencoders. In *IEEE/CVF Conference on Computer Vision and Pattern Recognition (CVPR)*, pages 16133–16142, 2023.
38. Ekin D. Cubuk, Barret Zoph, Jonathon Shlens, and Quoc V. Le. Randaugment: Practical automated data augmentation with a reduced search space. In *CVPRW*, pages 702–703, 2020.